# On the implementation of computed laminography using synchrotron radiation

L. Helfen,[1,a)] A. Myagotin,[1,2] P. Mikulík,[3] P. Pernot,[1,b)] A. Voropaev,[2] M. Elyyan,[1] M. Di Michiel,[4] J. Baruchel,[4] and T. Baumbach[1,5]

[1]*Institut für Synchrotronstrahlung (ISS/ANKA), Karlsruhe Institute of Technology (KIT), D-76128 Karlsruhe, Germany*
[2]*Saint-Petersburg State University of Civil Aviation, 196210, Saint-Petersburg, Russia*
[3]*Department of Condensed Matter Physics, Faculty of Science, Masaryk University, CZ-61137 Brno, Czech Republic*
[4]*European Synchrotron Radiation Facility (ESRF), F-38043 Grenoble, France*
[5]*LAS, Karlsruhe Institute of Technology, D-76128 Karlsruhe, Germany*

Hard x rays from a synchrotron source are used in this implementation of computed laminography for three-dimensional (3D) imaging of flat, laterally extended objects. Due to outstanding properties of synchrotron light, high spatial resolution down to the micrometer scale can be attained, even for specimens having lateral dimensions of several decimeters. Operating either with a monochromatic or with a white synchrotron beam, the method can be optimized to attain high sensitivity or considerable inspection throughput in synchrotron user and small-batch industrial experiments. The article describes the details of experimental setups, alignment procedures, and the underlying reconstruction principles. Imaging of interconnections in flip-chip and wire-bonded devices illustrates the peculiarities of the method compared to its alternatives and demonstrates the wide application potential for the 3D inspection and quality assessment in microsystem technology. © *2011 American Institute of Physics*. [doi:10.1063/1.3596566]

## I. INTRODUCTION

Using hard x rays generated by synchrotron accelerators, computed tomography (CT) profited from new possibilities for three-dimensional (3D) microstructural imaging of most diverse specimens.[1–3] This arises from several advantages provided by synchrotron radiation (SR) over x rays from laboratory sources such as x-ray tubes. Monochromatic radiation, a variety of contrast mechanisms (e.g. based on absorption, Fresnel diffraction or x-ray fluorescence) and coherence properties enabled efficient element-sensitive imaging[4,5] and quantitative electron-density imaging.[6–9] Due to the high photon flux, a higher spatial resolution than in laboratory imaging can usually be achieved for equivalent exposure times, either *via* miniaturization of the effective pixel sizes of x-ray sensors or by employing x-ray magnification techniques. However, as a consequence, the effective field of view of the detector system at the specimen position becomes reduced simultaneously.

For artefact-free reconstruction, however, CT requires non-truncated projections, i.e., the entire illuminated specimen volume should stay within the detector's field of view during a full tomographic rotation. In local tomography[10] this can be relaxed to a certain extent depending on the specimen, but for laterally extended specimens this requirement often implies that the regions of interest (ROI) must be extracted – usually by cutting or machining a small sample (e.g., a cylinder) out from the specimen – to perform the CT scans on these samples. Such sample extraction, however, can be considered as a serious drawback for a method to be used for a *nondestructive* inspection. Even if sample extraction succeeds without deterioration of significant parts of the sample volume, some samples may not provide sufficient mechanical stability for performing the CT scan. Also from an engineering perspective, being able to satisfy local boundary conditions or to apply engineering-relevant loads is of great importance.

We have developed laminographic imaging using synchrotron radiation[11] which is adapted to experimental setups with a parallel-beam geometry and fixed source/detectors. Using optimized filtering of the 2D projection data, the developed method of computed laminography (CL) profits from the numerous advantages of SR mentioned before. Several papers have already appeared on SR-CL, e.g., focussing on the very principles of the technique[11,12] and the use of different x-ray contrast modes.[12,13] In addition, the technique was recently adapted to neutron imaging[14] where similar instrumental constraints exist. Originally, the driving force behind SR-CL was nondestructive inspection of microsystem devices,[15,16] but recently the method has been spread into new application fields like cultural heritage,[17,18] paleontology,[19] and materials science.[20,21] This spreading of the technique into very different fields of investigation and the increase in quality of the reconstructed images, since the first demonstration experiments,[11] can be mainly attributed to (1) improved image reconstruction techniques and (2) significant improvements of the instrumental implementation to increase the precision in specimen scanning and to facilitate time-efficient user experiments.

a)Also at ESRF. Electronic mail: lukas.helfen@kit.edu.
b)Present address: ESRF.

This paper is dedicated to the basics of the technique, to the principal differences with respect to similar tomosynthesis implementations,[22,23] to the data reconstruction and evaluation procedure, and to describe possible instrumental implementations. As will be shown, the latter can indeed be rather similar to the ones used for CT, and thus, both setups can be combined in a single multipurpose instrument. Including, also, remarks about the instrument alignment, it may serve as a guidance to the reader for his own instrumental implementations. Examples from the original scope of the method, nondestructive 3D imaging of microsystem devices, and microelectronics, are used for an intuitive illustration.

## II. EXPERIMENTAL METHOD

Laminography or classical tomography (termed "classical," "conventional," or "analog" after the widespread introduction of computed tomography) is based on the acquisition of an integrated image during a synchronized motion of the x-ray source, detector, and/or specimen.[24,25] This means that the 2D detector (e.g., x-ray film) is exposed and integrates the intensity during such a synchronous motion. The imaging geometry defines a particular focal plane *parallel to the detector plane* which is imaged sharply, since specimen features on this plane are projected during the synchronous scanning motion always to the same points on the detector. All other specimen planes are blurred out with increased blurring for growing distances from such a focal plane. This acquisition scheme can be extended to the acquisition of multiple focal planes in a single scan, if a finite number (e.g., 5) of semi-transparent detectors are employed (e.g., arrangements of multiple x-ray films[26] were proposed).

Tomosynthesis (TS) is an imaging technique where multiple distinct exposures are made by the x-ray detector during a scanning motion. For 3D reconstruction, the radiographs (e.g., the developed x-ray films) are optically back-projected onto a viewing screen which allows any arbitrary slice to be investigated. After digital x-ray detectors became widely available, this procedure has been developed further towards digital tomosynthesis (DTS) where the optical backprojection is replaced by a numerical procedure. In order to bring any desired specimen plane into focus,[25] the algorithms use mostly shifting and summation[27] of the acquired digital radiographic images. In many implementations of DTS, filtering of the projection data is not applied and the image is superimposed by a strong low-frequency component which limits faithful detection of details. Adapted digital filtering techniques can be employed to suppress these low-frequency components but there still remains (e.g., in comparison to cross sections from CT) a certain blur of a given plane by out-of-plane features in the specimen.

In medical imaging, for obvious reasons, the patient usually is stationary, and source and detector are moved. There exist many imaging and scanning geometries developed for tomosynthesis and laminography, e.g., where detector and source move on straight lines (linear tomosynthesis) or on circles (circular tomosynthesis) and also many different approaches for image reconstruction like simple shift-and-add approaches up to more stringent algebraic reconstruction

techniques. Also, sometimes, projections are resorted to profit from instrumentally more simple methods. One variation of computed laminography[24] exploits the divergent fan beam geometry of an x-ray tube source, and the specimen is moved on a linear trajectory through this fan beam in order to extract projections by resorting the data acquired.

### A. Choice of the scanning geometry

Many of these approaches are not adapted to imaging at large-scale facilities such as synchrotron light sources. The beam divergence hardly exceeds some mrad even when using focussing devices, which severely limits the directions available from the geometry using data resorting procedures. Furthermore, the sources are not amenable to be rotated around the specimen. This entails a rotation of the specimen itself in order to acquire the projection data from different (viewing) directions.

Nevertheless, some of the approaches described before were recently adapted to the specificities of SR. Using the scanning geometry of classical laminography or circular tomosynthesis, CL using SR was developed[11] using a filtered-backprojection approach. Also more traditional digital tomosynthesis methods using a scanning geometry similar to limited-angle CT with detector rotation during a scan[22] and variants with a stationary detector now involving "shrink-shift-and-add" operations (to account for the in general non-parallel alignment of specimen and detector) were reported.[23]

We will concentrate on the approach of SR-CL in the following since it is instrumentally rather simple, and thus allows for high-spatial resolution to be attained. It can be easily combined into a setup allowing both laminography and CT. SR-CL employs a scanning scheme which is isotropic in the in-plane directions of the specimen yielding the same resolution and sensitivity in all directions perpendicular to the rotation axis. Due to this isotropy, SR-CL can be expected to give superior results compared to limited-angle SR-CT, especially if the accessible angular ranges are restricted either due to mechanical limitations (collision between specimen and detector/source) or due to insufficient x-ray transmission. Below $\sim \pm 70°$ angular CT scanning range (corresponding to $\theta = 70°$), cf. Fig. 1, we expect significant advantages for CL. The advantage of CT is that the optimum angle has not to be known in advance but could be determined, if there are no "hard" mechanical limitations, from the entire projection series acquired.

In order to easily integrate it into imaging setups at synchrotron beamlines, we adopt similar principles as in SR-CT, i.e., involving a stationary detector and only specimen rotation. On the other hand, reconstruction will not be easily amenable to "shift-and-add" methods and its variants but requires more sophisticated methods, such as 3D volume filtered backprojection, direct Fourier inversion, or algebraic reconstruction techniques.

In fact, SR-CL can be understood as a more generalized version of SR-CT. The latter consists in the acquisition of projection datasets of an object and rotation of the object around the tomographic axis, which is perpendicular to the
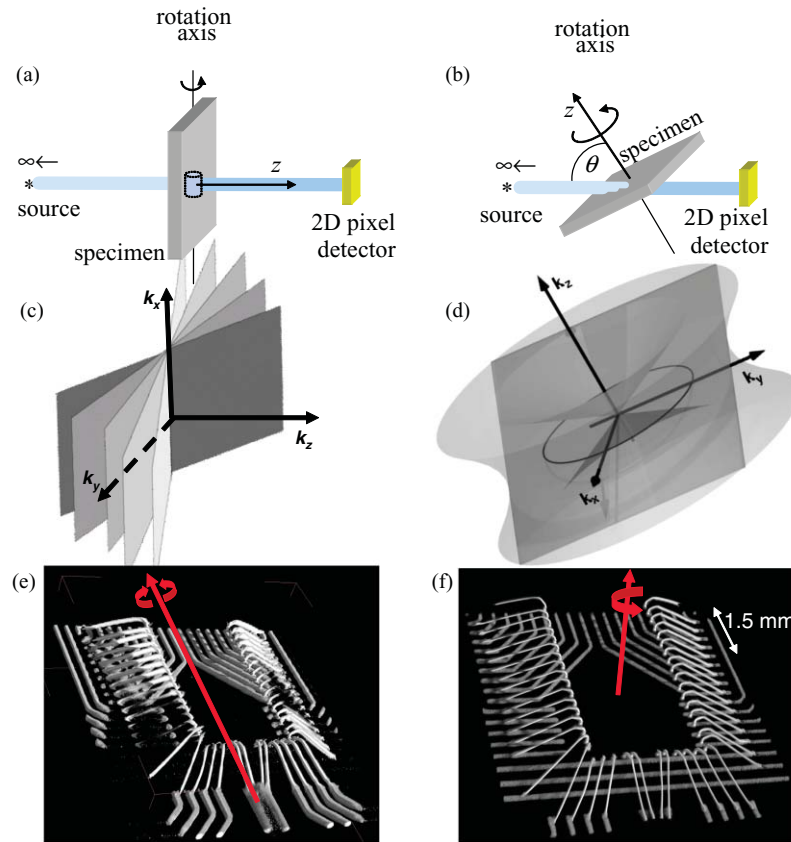
FIG. 1. (Color online) Comparison of the scanning geometries of limited-angle SR-CT and SR-CL in real space (a and b) and in the Fourier domain of the specimen (c and d) for a parallel-beam geometry. Their capabilities for imaging of a wire-bonded integrated circuit (encapsulated in a glob top), both recorded with $E = 20.5$ keV and a detector pixel size of 5 $\mu$m, are illustrated in (e) and (f). The metalizations and wires perpendicular to rotation axis are not faithfully reproduced by limited-angle CT (e), while being well reproduced by SR-CL (f). For both experiments, equivalent angular scanning ranges of $\pm 60°$ and $\theta = 60°$, respectively, were chosen.

transmitted x-ray beam (see Fig. 1(a)). For large source-specimen distances, the imaging geometry can be well approximated by a parallel beam[28] incident on the specimen which enables artefact-free reconstruction of any plane along the rotation axis. Additionally, the projections must not be truncated to avoid artefacts, i.e., the specimen must be less extended than the effective field of view of the 2D detector in all directions perpendicular to the rotation axis, resulting in a cylindrical envelope as maximum specimen extension, as sketched in Fig. 1(a).

For SR-CL[11] the tomographic axis is inclined (see Fig. 1(b)) by the so-called laminographic angle $\theta < 90°$ (where $\theta = 90°$ corresponds to the scanning geometry of CT). Assuming a monochromatic parallel x-ray beam and ideal detector response, the transmitted intensity distribution $I_T$ for a given projection direction can be described by

$$I_T(u, v)/I_0(u, v) = \exp(-p(u, v))$$

$$= \exp\left[-\int \mu(u, v, z')dy_w\right], \quad (1)$$

where $I_0$ corresponds to the incident intensity, $p$ denotes the projection of the spatial distribution of the linear attenuation coefficient $\mu$, and $(u, v)$ are the coordinates parallel to the detector plane, perpendicular to the optical axis $y_w$. In order to reconstruct the sample interior with minimized artefacts, one requires reliable radiographic data from the ROI

with optimized and preferably similar average transmission values $\langle I_T(u, v)/I_0(u, v) \rangle$ for all radiographic directions acquired. The inclined geometry described above is particularly adapted to flat specimens of dimensions exceeding the field of view provided by the detector: the (on average across the projection images) similar thickness of the specimen along the beam direction minimizes the variance of the average x-ray transmission on the detector during a scan.

This is very different in comparison to limited-angle CT, where the average transmission is maximum in directions parallel to the specimen normal and tending towards zero for large absorbing specimens in directions perpendicular to it. This inherently limits the range of projection angles which contribute reliable data for the reconstruction.

In the 3D Fourier domain of the specimen, only two wedges around the specimen rotation are sampled for CT (see Fig. 1(c)). Outside these regions, no information about the specimen is available. The coverage of the 3D Fourier domain by SR-CL is much larger and isotropic around the specimen through-plane directions (see Fig. 1(d)).

The effect on the reconstruction quality is illustrated by the example of a wire-bonded device protected by a coating resin (a so-called glob top) against mechanical and environmental hazard. Limited-angle CT in Fig. 1(e) shows that most extended structures (i.e., metallization lines on the substrate and bonding wires) perpendicular to the rotation axis

(red arrow) are missing which results from insensibility towards low spatial frequencies (within the missing wedges) along these directions. Due to the isotropy of scanning perpendicular to the rotation axis and the larger coverage of the 3D Fourier domain, SR-CL in Fig. 1(f) reproduces these structures much better; one does not notice any artefacts around the wires or the metallization lines. These examples were reconstructed by filtered backprojection (see Sec. II D for further reference).

### B. Instrumentation

In the following we describe the setups used for developing the technique and the resulting instrument which is used for user experiments. The method's development was done at the imaging beamline ID19 of the ESRF[29] and resulted in a concept which is now used at ESRF's high-energy beamline ID15.[30] Having demonstrated its capabilities to attain high spatial resolution down to the $\mu$m scale and ease of use, this concept is being retained for further instruments which are under construction at KIT's ANKA storage ring and shall be available in the near future.

The common point between these setups consists in the use of a standard compact rotation table where the specimen is held by a transparent (i.e., weakly absorbing) holder at a certain distance in order to allow the beam passing the rotation platform. The distance of the specimen to the rotation platform should be minimized in order to reduce the specimen run-out due to the wobble error motion of the rotation table (i.e., the excentricity at the specimen position) but elevated enough that no shadowing of the x-ray beam by any part of the rotation table or specimen holder occurs. The tilt angle $\theta$ of the rotation axis is performed by a simple wedge mounted on a goniometer by which the exact tilt angle can be adjusted.

Depending on the goniometer's geometry and travel, different configurations may be implemented. In cases where the goniometer's angular range is rather restricted, a wedge providing almost the complete tilt angle (e.g., 30° to achieve a certain averaged x-ray transmission) may be required. This means that one is restricted in the tilt angle to the wedge angle plus minus half the travel. In cases where the tilting range is considerable (e.g., ±15°), one might envisage extending the angle by a smaller wedge angle within the travel range (e.g., 15°) and the CT imaging mode can be attained by moving the goniometer tilt to −15° while tilt angles up to 30° can be attained by moving towards +15°.

Figure 2 shows the two configurations both schematically as well as a photograph from setups realized. In both implementations, the laminographic angle $\theta$ is adjusted via a commercial goniometer tilting stage which could be replaced by Eulerian cradles or an L-arm driven by a conventional rotation stage.

In the implementation of Fig. 2(a), the specimen holder consists in a tube made from PMMA. The specimen translations are realized by a simple goniometer head designed for diffractions experiments and do not provide long travel for large specimens.

In the implementation used for high-energy experiments at beamline ID15 shown in Fig. 2(b), the specimen holder
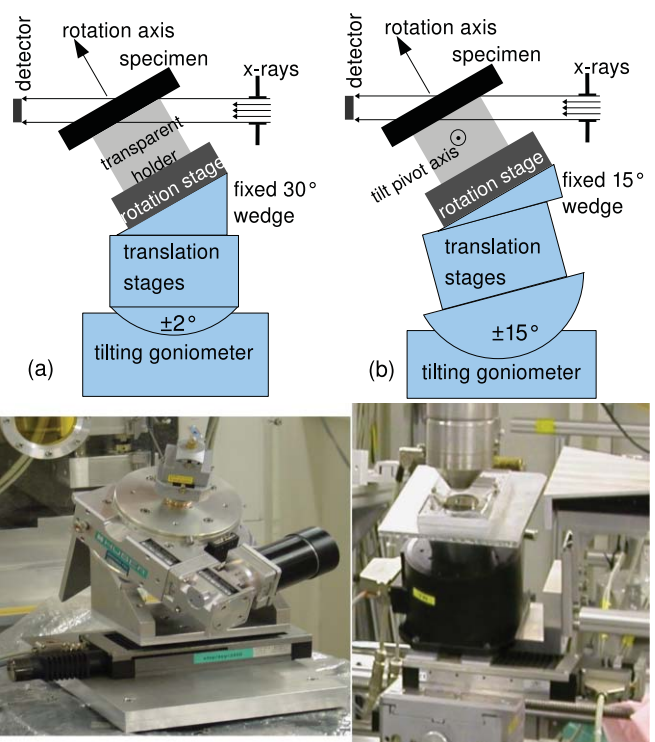


FIG. 2. (Color online) Schematic drawings and photos of experimental setups for SR-CL, allowing only SR-CL (a) with a short-range tilting stage and enabling both SR-CL and SR-CT (b) by means of a long-range tilting stage. The tilt pivot axis is the rotation axis of the tilting goniometer which should be perpendicular with respect to the transmitted beam direction (i.e., a vector out of the drawing).

consists of an aluminium cone carrying a ferromagnetic platform which holds a magnetic specimen frame. A long translation stage (towards the right in the photograph) which is retracted during the laminographic scans allows one to position the specimen with maximum lateral extensions of 10 cm by a pushing motion.

For both configurations, the rotation stage can be translated laterally (by a long-travel translation stage perpendicular to the beam direction) to move the specimen out of the beam. In this way, beam reference images can be acquired which are used for intensity normalization according to Eq. (1).

From the point of view of the measurement, the rotation axis, the tilt pivot axis, and the centre of the specimen ROI would ideally meet in a common point, so that a change of the laminographic angle does not involve a repositioning of the rotation axis or the specimen. For positioning or scanning the specimen in the through-plane direction or reasons of alignment, respectively, it can be beneficial to translate the specimen or alignment target along the rotation axis by a dedicated translation stage.

### C. Instrument alignment

As for most tomographic techniques, it is important to align the instrument axes with respect to the direction of the transmitted beam. In parallel-beam CT at synchrotron beamlines, one can significantly speed up the reconstruction,[27,31] if one aligns also projection of the rotation axis onto the

detector plane and the detector lines or rows to 90°. In this case, the 3D reconstruction problem can be split up into the reconstruction of a series of 2D cross-sectional slices. Then, the projection information needed for the reconstruction of a given slice can be extracted from the same detector line for all projection angles.

The same does not apply to SR-CL, since for any given slice to be reconstructed there are many projections where a 2D region is required as input data. This means that the exact alignment angle is not important, but the angle should be known to a precision determined by the pixel resolution of the 2D detector. For the case of a square $1024 \times 1024$ pixel detector, (i.e., if one tolerates a maximum angular misalignment of one pixel over the detector width of 1024 pixels) the angles between the projection of the rotation axis onto the detector plane and the detector rows/columns must be known with an accuracy of around 1 mrad. A similar estimation can also be made for the angle between the rotation axis and the beam direction.

The instrumental configuration illustrated in Fig. 2(b) allowing both CT and CL is much easier to align than the configuration where only the inclined axis is available, represented by Fig. 2(a). We usually start with the alignment of the CT case, i.e., when the rotation axis is perpendicular to the transmitted beam. First, a needle is placed on the specimen rotation stage and turned by 180°. In a parallel-beam geometry, the image taken at 180° is a mirror image of the image taken at 0°. Image correlation techniques can be used to determine the tilt and lateral position of the rotation axis on the detector. The detector is turned and the rotation axis translated laterally until the rotation axis is perpendicular to the detector lines and in the image centre.

Then, a point object (e.g., a small spherical metal ball) is placed out of the rotation centre of the tilting goniometer in such a way that it is on the same height (with respect to the beam) for both the CT and the CL cases. The position away from the rotation centre entails a translation along the beam direction which can be used to align the tilt pivot axis (see Fig. 2(b) where the pivot axis is below the specimen plane) perpendicular to the beam: by tilting the rotation axis between the two cases (CT and CL), the tilting goniometer has to be turned (e.g., by a dedicated rotation underneath) until there is no lateral shift on the detector between the CT and CL positions.

By iteratively performing the two adjustments, one usually rather quickly approaches the desired alignment state. The exact tilting angle of the rotation axis can be determined by placing the point object (metal ball) out of the rotation centre of the rotation axis, so that it does not move out of the detector field of view during a scan. Due to our previous alignment, it will follow an ellipse on the detector whose principal axes are parallel to the detector lines/rows. The ratio of the minor axis to the major axis of the ellipse can then be used to calculate the exact axis inclination angle.

Slow drifts (e.g., due to temperature changes) mostly affect the mutual position of specimen and detector, so that over the time of a few scans the position of the projection of the specimen rotation centre (determined by the rotation axis) may shift with respect to the detector centre. In order
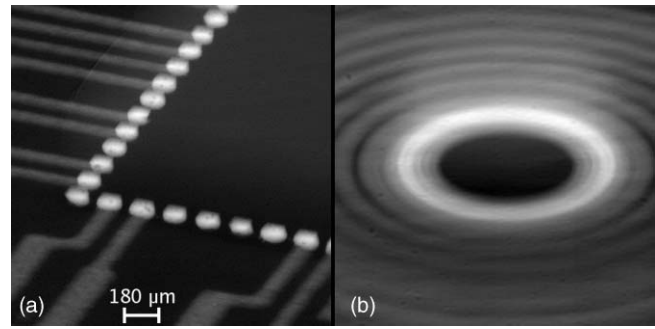


FIG. 3. Single projection image (a) of the corner of an integrated circuit flip-chip bonded to a substrate and image obtained via an integration over 1800 of such images acquired during a scan (b). For the parallel-beam geometry, the latter consists of a superposition of ellipses of variable size along the projection of the rotation axis onto the detector plane.

to calculate the rotation centre with sub-pixel precision (a parameter needed for the 3D reconstruction), we generate from the 2D projection data an integrated image by summation of all individual projections. Since every feature in the specimen follows an ellipse on the detector plane, we obtain a superposition of ellipses of different radius and different off-set along the rotation axis. If the projection of the rotation axis onto the detector plane is perpendicular to the detector lines, the integrated image is symmetric along the horizontal axis. For illustration, a single projection and a resulting integrated image are shown in Fig. 3 for a flip-chip bonded device. Using standard image correlation techniques, the rotation axis can be determined to sub-pixel precision between the integrated image and a horizontally flipped derivative.

### D. Image reconstruction by filtered backprojection

In general an analytic reconstruction procedure for the spatial distribution of the linear attenuation coefficient $\mu(x, y, z)$ consists of two principal steps: generation of a 3D *compound image* and its convolution with an *inverse filter function*.

In the case of computed laminography the orientation of a projection beam in 3D space is defined by a tomographic rotation $\phi$ and the laminographic angle $\theta$. The latter is measured between the object rotation axis $z$ and beam direction $y_w$ as it is shown in Fig. 4. Using the same definitions as in Eq. (1), the compound image $g(x, y, z)$ is obtained by a so-called *backprojection process* which smears every radiographic projection $p_{\phi,\theta}(u, v)$ along the same trajectory in the reconstruction space as the projection was measured initially. More formally

$$g(x, y, z) = \int_0^{2\pi} g_{\phi,\theta}(x, y, z) d\phi, \qquad (2)$$

where $g_{\phi,\theta}$ denotes a 3D image in the Cartesian real-space coordinate system $(x, y, z)$ obtained by the backprojection of a single projection under the inclination angles $\theta$ and $\phi$ with respect to the $z$ axis:

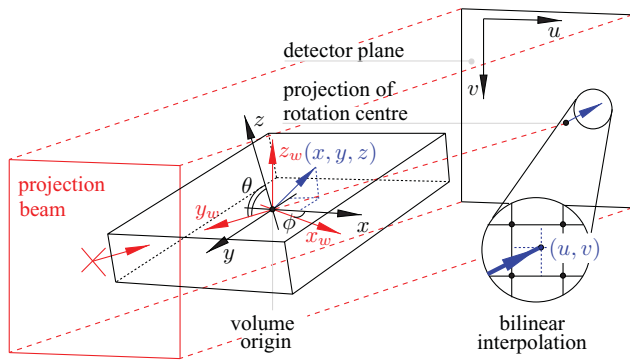$$g_{\phi,\theta}(x, y, z) = p(T_{\phi,\theta} \cdot (x, y, z)^T).$$

FIG. 4. (Color online) Illustration of 3D backprojection for the parallel-beam geometry. The correspondence between voxel positions $(x, y, z)$ in the reconstructed volume and detector pixels $(u, v)$ can be established via the matrix formulation of Eq. (3).

Here the transformation matrix $T_{\phi,\theta}$ is of form

$$T_{\phi,\theta} = \begin{bmatrix} \cos\phi & \sin\phi & 0 \\ \cos\theta \cdot \sin\phi & -\cos\theta \cdot \cos\phi & \sin\theta \end{bmatrix}, \quad (3)$$

which for the given angles $\phi$ and $\theta$, maps 3D coordinates $(x, y, z)$ of the reconstructed volume to the coordinates $(u, v)$ of the detector plane. In practice, the projection images are sampled at discrete points and the value of $p_{\phi,\theta}$ at the position $(u, v)$ should be estimated by an interpolation. For the interpolation, one can apply for instance a 2D sinc function or the nearest-neighbor approach. Due to the tradeoff between computational effort and interpolation precision, we chose a bilinear interpolation scheme.

A relation between the compound image and the unknown attenuation function $\mu$ can be modeled by[32]

$$g(x, y, z) = \{h \otimes \mu\}(x, y, z),$$

where $h$ denotes a 3D point spread function; $\otimes$ is a 3D convolution. It should be noted that the function $h$ describes both projection and backprojection processes and depends solely on the experimental geometry. Using the Fourier representation of the above equation, one gets a reconstruction equation:

$$\mu(x, y, z) = \mathcal{F}^{-1}\{\mathcal{M}(\mathbf{k})\}$$
$$= \mathcal{F}^{-1}\{\overline{\mathcal{H}}(\mathbf{k})\mathcal{G}(\mathbf{k})\} = \{\bar{h} \otimes g\}(x, y, z), \quad (4)$$

where $\bar{h} = \mathcal{F}^{-1}\{\overline{\mathcal{H}}\} = \mathcal{F}^{-1}\{1/\mathcal{H}\}$ is a 3D inverse filter function, $\mathcal{M}$ is the 3D Fourier transform of $\mu$ and $\mathbf{k} = (k_x, k_y, k_z)$ is the Fourier conjugate to the real-space vector $(x, y, z)$ of a coordinate system fixed to the specimen. From earlier calculations,[33] an explicit form of the function for the laminographic geometry can be expressed in cylindrical coordinates as[32, 34]

$$\overline{\mathcal{H}}(k_p, k_\phi, k_z)$$

$$= \begin{cases} \frac{\sin\theta}{2}\sqrt{k_p^2 - k_z^2 \cdot \cot^2\theta} : k_p \geq |k_z| \cdot \cot\theta, \\ 0 : \quad \text{elsewhere,} \end{cases} \quad (5)$$

with $k_p = \sqrt{k_x^2 + k_y^2}$ and $k_\phi = \arctan(k_y/k_x)$. Reconstruction according to Eq. (4) defines a so-called *filtering after backprojection* approach (i.e., the inverse filter is applied after the

computation of the compound image) which is impractical for the implementation due to a high computational complexity of the 3D convolution.

The *filtering before backprojection* approach is based on the following property:[35]

$$\{\mathcal{G}_{\phi,\theta} \cdot \bar{\mathcal{H}}\}(\mathbf{k}) = \{\mathcal{P}_{\phi,\theta} \cdot \bar{\mathcal{H}}_{\phi,\theta}\}(T_{\phi,\theta} \cdot \mathbf{k}) \cdot \delta(T_{\phi,\theta}^{\perp} \cdot \mathbf{k})$$

i.e., the 3D convolution of the backprojection image with the inverse filter function can be replaced by a convolution of projection $\mathcal{P}_{\phi,\theta}$ with a 2D inverse filter $\bar{\mathcal{H}}_{\phi,\theta}$ (in the above formula $\delta$ corresponds to a Dirac delta function). Thus for a set of $M$ projection images the reconstruction procedure reduces to the evaluation of the following sum:

$$\mu(x, y, z) = \frac{1}{M} \sum_m q_{\phi_m,\theta}, \quad (6)$$

where $q_{\phi,\theta}(u, v) = \{\bar{h}_{\phi,\theta} \otimes p_{\phi,\theta}\}(u, v)$ is a filtered projection image and the discrete angular positions are $\phi_m = 2\pi m/M$. Using the relationships $k_u = k_p$ and $k_v = k_z/\sin\theta$ for the frequency coordinates in the detector coordinate system (see Fig. 4), the 2D inverse filter function to be applied to the projections can be immediately derived[35] from Eq. (5) yielding

$$\mathcal{F}\{\bar{h}_{\phi,\theta}\} = \overline{\mathcal{H}}_{\phi,\theta}(k_u, k_v) = \frac{\sin\theta}{2} \cdot |k_u|. \quad (7)$$

For the case of CT when the rotation axis $z$ is perpendicular to the transmitted beam ($\theta = \pi/2$), the obtained filter converges to the conventional Ram–Lak function[36, 37] (i.e., a ramp filter multiplied with low-pass step function). The filter depends neither on the rotation angle $\phi$ nor on the coordinate $k_v$ along the projection axis on the 2D detector (i.e., the row index for a projection of the rotation axis onto the detector plane which is vertical). Thus, if the rotation axis is perpendicular to the detector lines, the projection filtering can be efficiently implemented by a series of 1D fast Fourier transforms.

## III. EXAMPLES

In Fig. 1, a reconstruction of a wire-bonded device by SR-CL was shown which illustrates the capabilities for 3D imaging of microsystem devices. In comparison to limited-angle CT, SR-CL yields better results due to a more isotropic scanning around the through-plane direction of the specimen.

Compared to tomosynthesis techniques based on "shift-and-add" approaches for reconstruction, the addition of the projection filtering step improves the reconstructed images significantly. This is demonstrated by the example of a flip-chip bonded device in Fig. 5 which was reconstructed from the same input projection data (cf. Fig. 3 for an example of a single projection) once according to Eq. (2) without the filtering step (left) and once according to Eq. (6) with projection filtering (right). In fact, unfiltered backprojection corresponds to shift-and-add approaches[25] which merely sum up different (shifted and, possibly, shrinked) radiographs or projections. From the reconstructed cross-sectional slices we see that filtered backprojection shows much more detail than unfiltered backprojection, which is spoilt by overrepresented low spatial
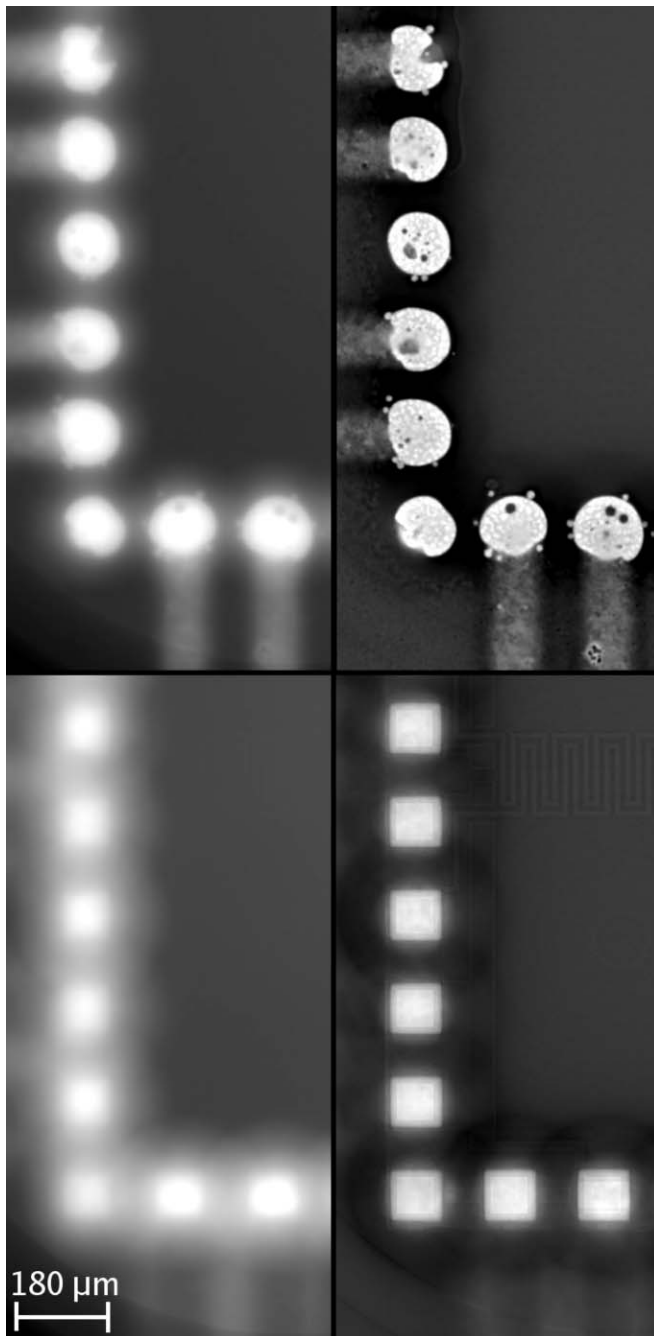
FIG. 5. Comparison of reconstructed cross-sectional slices via unfiltered (left) and filtered backprojection (right) using the example of a corner of a flip-chip bonded device. Two different slices are shown, namely, the interface towards the printed circuit board (top) with its Cu conduction lines and the interface towards the integrated circuit (bottom). For the filtered backprojection approach, Al metallization lines and connection pads can be discerned on the IC surface. Also, the metallographic microstructure of the bumps of different phases is clearly visible. The two slices are 53 $\mu$m apart, and the solder bump pitch is 180 $\mu$m.

frequencies (see the images on the left-hand side). There is a significant improvement on the reconstruction quality visible in these images (i.e., the microstructure of the bump is well discernable) if one compares them to the first publications on SR-CL, e.g., Fig. 5 from Ref. 11. We attribute this both to a higher mechanical precision of the instrument axes and to

the improved reconstruction using the ideal filter function in filtered backprojection.

## IV. CONCLUSIONS

Summarizing, we motivated the choice of the scanning geometry for SR-CL and introduced the basic principles of the experimental setup and reconstruction procedure. The method has considerable advantages compared to limited-angle CT which was demonstrated by the example of a microelectronic device. SR-CL can thus be successfully used for high-resolution 3D imaging of microstructures in absorbing material plates/sheets or in laterally extended devices. We implemented suitable projection filtering methods for 3D backprojection which deliver highly detailed reconstructed images compared to unfiltered backprojection which can be considered as an equivalent of "shift-and-add" methods traditionally used in digital tomosynthesis techniques.

Different instrumental setups installed at ESRF beamlines ID19 and ID15 – and soon also available at ANKA – allow for systematic device inspection by combination of full-field imaging and lateral specimen scanning over large areas. This enables three-dimensional imaging with variable spatial resolution of hidden defects and components (e.g., packaging or interconnects) in microsystem devices or of the microstructure of materials.

[1] S. Stock, Int. Mater. Rev. **53**, 129 (2008).
[2] *Advanced Tomographic Methods in Materials Research and Engineering*, edited by J. Banhart (Oxford University Press, New York, 2008).
[3] P. Tafforeau, R. Boistel, E. Boller, A. Bravin, M. Brunet, Y. Chaimanee, P. Cloetens, M. Feist, J. Hoszowska, J. Jaeger, R. F. Kay, V. Lazzari, L. Marivaux, A. Nel, C. Nemoz, X. Thibault, P. Vignaud, S. Zabler, Appl. Phys. A: Mater. Sci. Process. **83**, 195 (2006).
[4] R. Cesareo, A. L. Hanson, G. E. Gigante, L. J. Pedraza, and S. Q.G. Mathaboally, Phys. Rep. **213**, 117 (1992).
[5] F. A. Dilmanian, X. Y. Wu, E. C. Parsons, B. Ren, J. Kress, T. M. Button, L. D. Chapman, J. A. Coderre, F. Giron, D. Greenberg, D. J. Krus, Z. Liang, S. Marcovici, M. J. Petersen, C. T. Roque, M. Shleifer, D. N. Slatkin, W. C. Thomlinson, K. Yamamoto, Z. Zhong, Phys. Med. Biol. **42**, 371 (1997).
[6] K. A. Nugent, T. E. Gureyev, D. F. Cookson, D. Paganin, and Z. Barnea, Phys. Rev. Lett. **77**, 2961 (1996).
[7] P. Cloetens, W. Ludwig, J. Baruchel, D. van Dyck, J. van Landuyt, J. Guigay, and M. Schlenker, Appl. Phys. Lett. **75**, 2912 (1999).
[8] D. Paganin, S. C. Mayo, T. E. Gureyev, P. R. Miller, and S. W. Wilkins, J. Microsc. **206**, 33 (2002).
[9] A. Paganin, *Coherent X-Ray Optics* (Oxford University Press, Oxford, 2006).
[10] A. Kyrieleis, V. Titarenko, M. Ibison, T. Connolley, and P. J. Withers, J. Microsc. **241**, 69 (2011).
[11] L. Helfen, T. Baumbach, P. Mikulík, D. Kiel, P. Pernot, P. Cloetens, and J. Baruchel, Appl. Phys. Lett. **86**, 071915 (2005).
[12] L. Helfen, T. Baumbach, P. Cloetens, and J. Baruchel, Appl. Phys. Lett. **94**, 104103 (2009).
[13] N. Watanabe, M. Hoshino, K. Yamamoto, S. Aoki, A. Takeuchi, and Y. Suzuki, J. Phys.: Conf. Ser. **186**, 012022 (2009).

[14]L. Helfen, F. Xu, B. Schillinger, E. Calzada, I. Zanette, T. Weitkamp, and T. Baumbach, "Neutron laminography - a novel approach to three-dimensional imaging of flat objects with neutrons," Nucl. Inst. Meth. A (in press).

[15]L. Helfen, A. Myagotin, P. Pernot, M. Di Michiel, P. Mikulík, A. Berthold, and T. Baumbach, Nucl. Inst. Meth. A **563**, 163 (2006).

[16]L. Helfen, A. Myagotin, A. Rack, P. Pernot, P. Mikulík, M. D. Michiel, and T. Baumbach, Phys. Status Solidi A **204**, 2760 (2007).

[17]K. Krug, L. Porra, P. Coan, A. Wallert, J. Dik, A. Coerdt, A. Bravin, M. Elyyan, P. Reischig, L. Helfen, T. Baumbach, J. Synchrotron Radiat. **15**, 55 (2008).

[18]J. Dik, P. Reischig, K. Krug, A. Wallert, A. Coerdt, L. Helfen, and T. Baumbach, J. Am. Inst. Conserv. **48**, 185 (2009).

[19]A. Houssaye, F. Xu, L. Helfen, V. D. Buffrénil, T. Baumbach, and P. Tafforeau, J. Vertebr. Paleontol. **31**, 2 (2011).

[20]A. J. Moffat, P. Wright, L. Helfen, T. Baumbach, G. Johnson, S. M. Spearing, and I. Sinclair, Scr. Mater. **62**, 97 (2010).

[21]F. Xu, L. Helfen, A. J. Moffat, G. Johnson, I. Sinclair, and T. Baumbach, J. Synchrotron Radiat. **17**, 222 (2010).

[22]D. Shimao, T. Kunisada, H. Sugiyama, and M. Ando, Jpn. J. Appl. Phys. **46**, L608 (2007).

[23]A. Maksimenko, T. Yuasa, M. Ando, and E. Hashimoto, Appl. Phys. Lett. **91**, 234108 (2007).

[24]S. Gondrom, J. Zhou, M. Maisl, H. Reiter, M. Kröning, and W. Arnold, Nucl. Eng. Des. **190**, 141 (1999).

[25]J. T. Dobbins III and D. J. Godfrey, Phys. Med. Biol. **48**, R65 (2003).

[26]B. G. Ziedses des Plantes, Acta Radiol. **13**, 182 (1932).

[27]R. Gordon and G. Herman, *International Review of Cytology*, (Academic, New York, 1974), Vol. 38, pp. 111–151.

[28]T. Weitkamp, P. Tafforeau, E. Boller, P. Cloetens, J.-P. Valade, P. Bernard, F. Peyrin, W. Ludwig, L. Helfen, and J. Baruchel, AIP Conf. Proc. **1234**, 83 (2010).

[29]T. Weitkamp, P. Tafforeau, E. Boller, P. Cloetens, J.-P. Valade, P. Bernard, F. Peyrin, W. Ludwig, L. Helfen, and J. Baruchel, AIP Conf. Proc. **1221**, 33 (2010).

[30]M. Di Michiel, J. M. Merino, D. Fernandez-Carreiras, T. Buslaps, V. Honkimäki, P. Falus, T. Martins, and O. Svensson, Rev. Sci. Instrum. **76**, 043702 (2005).

[31]S. Chilingaryan, A. Mirone, A. Hammersley, C. Ferrero, L. Helfen, A. Kopmann, T. dos Santos Rolo, and P. Vagovic, "A GPU-Based Architecture for Real-Time Data Assessment at Synchrotron Experiments," IEEE Trans. Nucl. Sci. (in press).

[32]G. Lauritsch and W. H. Härer, Proc. SPIE **3338**, 1127 (1999).

[33]H. Matsui, A. Iwata, I. Horiba, and N. Suzumura, IEEE Trans. Med. Imaging **12**, 307 (1993).

[34]L. Helfen, T. Baumbach, P. Pernot, P. Mikulík, M. Di Michiel, and J. Baruchel, Proc. SPIE **6318**, 63180N (2006).

[35]A. Voropaev, Master's thesis, Universität des Saarlandes 2009.

[36]G. Ramachandran and A. Lakshminarayanan, Proc. Natl. Acad. Sci. U.S.A. **68**, 2236 (1971).

[37]A. C. Kak and M. Slaney, *Principles of Computerized Tomographic Imaging* (IEEE Press, New York, 1988).